

MILLIMETER WAVELENGTH BRIGHTNESS FLUCTUATIONS OF THE ATMOSPHERE ABOVE THE SOUTH POLE

R. S. BUSSMANN^{1,2}

Department of Astronomy, University of Arizona, Tucson, AZ 85721

W. L. HOLZAPFEL¹

Department of Physics, University of California, Berkeley, CA 94720

AND

C. L. KUO³

Jet Propulsion Laboratory, Pasadena, CA 91125

To be submitted to ApJ

ABSTRACT

We report measurements of the millimeter wavelength brightness fluctuations produced by the atmosphere above the South Pole made with the Arcminute Cosmology Bolometer Array Receiver (ACBAR). The data span the 2002 Austral winter during which ACBAR was mounted on the Viper telescope at the South Pole. We recover the atmospheric signal in the presence of instrument noise by calculating the correlation between signals from distinct elements of the ACBAR bolometer array. With this method, it is possible to measure atmospheric brightness fluctuations with high SNR even under the most stable atmospheric conditions. The observed atmospheric signal is characterized by the parameters of the Kolmogorov-Taylor (KT) model, which are the amplitude and power law exponent describing the atmospheric power spectrum, and the two components of the wind angular velocity at the time of the observation. The KT model is typically a good description of the observed fluctuations, and fits to the data produce values of the Kolmogorov exponent that are consistent with theoretical expectations. By combining the wind angular velocity results with measurements of the wind linear velocity, we find that the altitude of the observed atmospheric fluctuations is consistent with the distribution of water vapor determined from radiosonde data. For data corresponding to frequency passbands centered on 150, 219, and 274 GHz, we obtain median fluctuation power amplitudes of [10, 38, 74] mK² rad^{-5/3} in Rayleigh-Jeans temperature units. Comparing with previous work, we find that these median amplitudes are approximately an order of magnitude smaller than those found at the South Pole during the Austral summer and at least 30 times lower than found at the ALMA site in the Atacama desert.

Subject headings: atmospheric effects — site testing — cosmic microwave background

1. INTRODUCTION

The geographic South Pole is one of the most important sites for astronomical observations at mm and sub-mm wavelengths. This is primarily due to the relatively high altitude and the lack of water vapor in the atmosphere. In addition, the stability of the atmosphere makes it especially well suited for observations of the cosmic microwave background (CMB) radiation. The recent detection of CMB polarization by DASI (Kovac et al. 2002) and fine scale CMB anisotropy measurements by ACBAR (Kuo et al. 2004, hereafter K2004) precede a wave of new instruments to be deployed at the South Pole in the next few years. Compared to balloon-borne experiments, ground based experiments can make use of larger mirrors and achieve longer continuous observation time. It was shown in Runyan et al. (2003) that the

background limited photon noise of the ACBAR experiment is only 50% more than that achieved in the balloon-borne BOOMERanG experiment (Crill et al. 2003). For many types of observations at the South Pole, atmospheric brightness fluctuations will not significantly increase the noise above the background limit.

The impact of atmospheric fluctuations on astronomical observations at mm wavelengths has been studied by several authors. Most of this work is concerned with distortions of the wavefront as the radiation propagates through the atmosphere and the effects this has on high resolution interferometry (e.g. Lay 1997). Previous studies of atmospheric brightness fluctuations at mm and cm-wavelengths have been limited by sensitivity (Wollack et al. 1997; Lay & Halverson 2000, hereafter LH2000). Furthermore, this is the first characterization of the atmospheric brightness fluctuations made during the Austral winter at the South Pole. It is expected that the fluctuation power will be lower than during the Austral summer due to lower ambient temperatures and lower precipitable water vapor.

We fit the observed atmospheric induced correlations between detectors in the ACBAR data with a Kolmogorov-Taylor (KT) model for the angular power

Electronic address: rsbusmann@as.arizona.edu
Electronic address: swlh@cosmology.berkeley.edu
Electronic address: clkuo@astro.caltech.edu

¹ Department of Physics, 361 LeConte Hall, University of California at Berkeley, Berkeley, CA 94720

² Department of Astronomy, University of California at Berkeley, Berkeley, CA 94720

³ Department of Physics, California Institute of Technology, Pasadena, CA 91125

spectrum of atmospheric fluctuations. The high SNR with which we measure the atmospheric fluctuations makes it possible to determine the amplitude and exponent of the KT power law and wind angular velocity for our atmospheric model. Combined with radiosonde measurements of wind linear velocity, we can infer the altitude at which the fluctuation signals arise. This work provides a detailed characterization of fluctuations in the atmosphere above the South Pole that can be used to compare sites and predict the performance of instruments and observation strategies.

In Section 2.1, we give a general overview of the environment of the South Pole as pertains to millimeter wavelength astronomical observations. Section 2.2 describes the spatial (Kolmogorov) and temporal (Taylor) components of the model. In Section 3, we detail the instrument specifications and explain the observing strategy. Sections 4 and 5 discuss the methodology used to process the data and compare to models for the atmospheric fluctuations. In Section 6, we present the results of this analysis, including the exponent of the power law, the amplitude of the fluctuations, measurements of the wind angular velocity, and the scale height of the fluctuations. Finally, in Section 7 we make some concluding remarks, including a comparison of our results with those obtained at the South Pole during the Austral summer and at the ALMA site in Chile.

2. ATMOSPHERE ABOVE SOUTH POLE

2.1. General Properties

The large scale air flow at the South Pole is dominated by a katabatic (moving downward due to cooling) wind from the Antarctic plateau driven toward the coast. At the South Pole Station, radiosonde meteorology measurements are taken twice a day during the summer, and once a day in winter. These data, which include the pressure, temperature, relative humidity, and wind angular velocity as a function of altitude, provide important information on the atmospheric properties. The weather data show that the surface wind direction is relatively constant, with higher wind speed in the winter than in the summer. It is also found that during the winter months, the cold surface creates a layer of temperature inversion where the air temperature rises from $\sim -60^\circ\text{C}$ at ice level to $\sim -40^\circ\text{C}$ at an altitude of approximately 200 m.

Using balloon-borne microthermal probes, Marks et al. (1999) found this temperature inversion layer to be turbulent. The AASTO team also confirmed this result with a non-intrusive SODAR system (Travouillon et al. 2003). The lack of radiative heating during the winter and the featureless landscape near the South Pole imply that the turbulence in the inversion layer is due to shear-induced instability. The high correlation between the horizontal wind speed and temperature fluctuation reported by AASTO also supports this point of view. The low-altitude atmospheric turbulence creates variations in the refraction index, and is of primary concern for optical seeing (Marks 2002; Travouillon et al. 2003).

Observations at mm wavelengths are limited by the emission of radiation by molecules in the atmosphere. The primary components of the air (O_2 and N_2) are very well mixed; these “dry” components produce a uniform

background of radiation that contributes photon noise to the detector. Water vapor in the atmosphere not only radiates at mm wavelengths, but also fluctuates in its mass fraction, resulting in brightness temperature fluctuations. Because of the low temperature immediately above the ground in the winter, the integrated water vapor pressure is small in the turbulent boundary layer ($<200\text{m}$).

In the optically thin limit, the water vapor contribution to sky brightness temperature is a function of the optical depth τ and thermodynamic temperature T ; in other words, it is proportional to the line of sight integral of water vapor pressure. Approximating the saturated water vapor pressure as an exponential function in T (following the Goff-Gratch equation⁴), the water vapor pressure profile can be derived from the publicly available archived radiosonde data.⁵ Fig. 1 shows the water vapor profiles measured with radiosonde data during 2002. Based on this data, we expect that the microwave radiation from water vapor at the South Pole comes predominantly from a thick layer between 0.3 km and 2 km above the ice.

One common way to characterize the quality of an observing site is to report the distribution of the integrated precipitable water vapor for an extended period of time. Previous studies of sky opacity in the sub-mm produced median precipitable water vapor levels at the South Pole of about 0.25 mm (Chamberlin & Bally 1994). The radiosonde data in Fig. 1 can be integrated to determine the precipitable water vapor for each day. Fig. 2 shows a histogram of the precipitable water vapor measurements over the 2002 Austral winter. The mean precipitable water vapor during winter is $0.26 \pm 0.2\text{mm}$. This is remarkably low when compared to the best six months

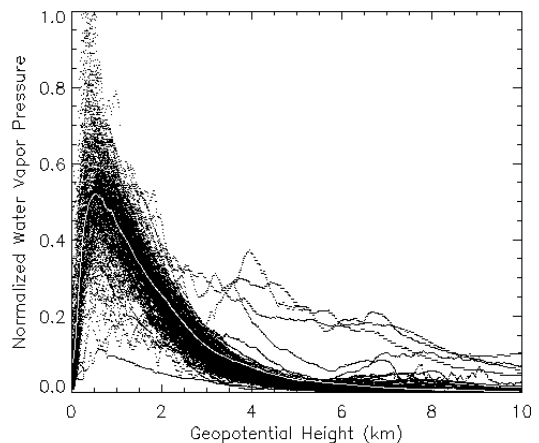


FIG. 1.— Water vapor pressure as a function of geopotential height above ice level at the South Pole as measured by radiosonde data, and normalized to the maximum observed value. Black lines represent water vapor pressure profiles for each day during the Austral winter; the white line is the average of all the profiles. Most of the water vapor pressure originates in a broad layer in the atmosphere between altitudes of 0.3 and 2 km. Anomalous profiles well above or below the average appear to be due to measurement errors.

⁴ <http://cires.colorado.edu/~voemel/vp.html>

⁵ <ftp://ice.ssec.wisc.edu/pub/raob/>

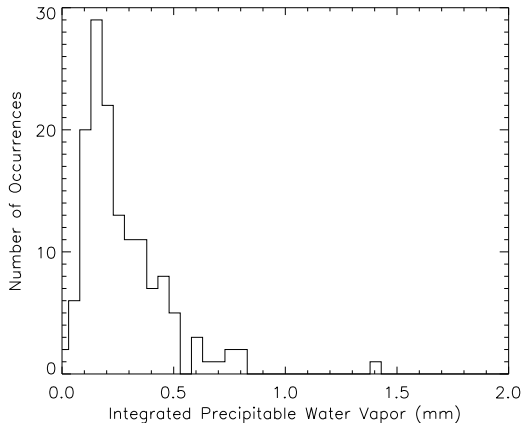


FIG. 2.— Distribution of integrated precipitable water vapor (in mm) at the South Pole for the 2002 Austral winter. The mean value of 0.26 mm is extremely small when compared to other well characterized astronomical sites.

at other well characterized sub-mm sites such as Mauna Kea (1.65 mm) and the Atacama desert (1.00 mm) (Lane 1998).

2.2. The Model

The Kolmogorov Turbulence (KT) model describes the cascade of turbulent energy from the large scales on which it is input, to the small scales where it is dissipated. Large scale turbulence in the atmosphere above the South Pole is produced by processes such as wind shear and convection. These processes produce fluctuations with scales that exceed or are comparable to the thickness of the turbulent layer. Eventually, the turbulent energy is dissipated on scales comparable to 1 mm, which are far smaller than we are capable of observing. The fluctuation angular power spectrum between the scales of energy injection and viscous dissipation, commonly known as the inertial subrange, is described by a power law with an exponent of $-11/3$. In the work described here, the scales being observed all lie in the inertial subrange and the fluctuation power should be well described by the KT model.

We assume the atmospheric signal seen by the telescope is dominated by fluctuations in a layer of turbulence with thickness Δh , located at height h above the ground. The telescope is pointed at an elevation angle ϵ , and the observed patch of sky subtends an angle of $\Delta\theta \sim 3^\circ$. Due to the relatively small size of the observed field and the typical altitude of the atmospheric water vapor,

$$\Delta h \gg \frac{h}{\sin \epsilon} \Delta\theta, \quad (1)$$

and it is safe to assume that we are observing the projection of the full 3-D Kolmogorov turbulence. In this limit, the thickness of the turbulent layer only affects the projected amplitude of the fluctuations. In addition, we are able to employ the small angle approximation ($\Delta\theta \ll 1$) and avoid the complexity of spherical harmonic functions. Under these assumptions, the angular power spectrum follows the 3-D isotropic KT power law

($P(k) \propto k^{-11/3}$), and can be parametrized as

$$P(\alpha) = B_\nu^2 \sin(\epsilon)^{-8/3} (\alpha_x^2 + \alpha_y^2)^{-b/2}, \quad (2)$$

where k is the spatial wave number, $\alpha = kh/\sin \epsilon$ is the angular wave number, and B_ν^2 is the amplitude fluctuation power at observing frequency ν (in GHz). From the KT model for atmospheric turbulence, we expect that $b = 11/3$; however, initially, we leave it as a free parameter in the model fitting. This is the same model used by Lay (1997) and LH2000 to characterize atmospheric brightness fluctuations. B_ν^2 is the amplitude of the power spectrum normalized to observations at the zenith and has units of $\text{mK}^2 \text{ rad}^{-5/3}$. We provide a more rigorous derivation of this relationship in Appendix A. The (instantaneous) angular correlation function is the Fourier transform of the angular power spectrum $P(\alpha)$:

$$\begin{aligned} C(\theta) &= \int d^2\alpha P(\alpha) e^{2\pi i \alpha \cdot \theta} \\ &= \int_0^\infty d\alpha \int_0^{2\pi} d\varphi \alpha P(\alpha) e^{2\pi i \alpha \theta \cos \varphi} \\ &= 2\pi \int_0^\infty d\alpha \alpha P(\alpha) J_0(2\pi \alpha \theta). \end{aligned} \quad (3)$$

To model the temporal variations, we follow the *frozen turbulence hypothesis* (FTH) proposed by Taylor (1938), which states that the small-scale turbulence velocity is much smaller than the global advection flow. In other words, the atmospheric fluctuations are modeled by a frozen pattern of fluctuations with Kolmogorov spectrum, blown through the experimental beams by a uniform wind. This model has been tested and verified by many groups engaged in interferometric observations. In the ACBAR observations, a chopping mirror sweeps the beam across the sky. In this case, applying FTH requires that the small scale turbulence velocity be much less than the sum of the chopper and wind angular speeds.

We expect the large scale air flow over a flat terrain like the South Pole plateau to be nearly horizontal. Indeed, Travouillon et al. (2003) report that the vertical wind speed is less than several tens of centimeter per second (compared to typical horizontal windspeeds on the order of 10 meters per second). In our model, we take the wind velocity \mathbf{v} to be completely horizontal.

3. OBSERVATIONS

The data used in this study were collected using the Arcminute Cosmology Bolometric Array Receiver (ACBAR, for a detailed description, see Runyan et al. (2003)): an instrument designed to measure the anisotropy of the CMB. ACBAR is an array of 16 bolometric detectors cooled to 240 mK with a 3 stage- ^3He sorption refrigerator. The square array is divided into four rows of four detectors each. The top and bottom rows correspond to 274 GHz and 219 GHz (bandwidths 48 and 31 GHz, respectively), while the middle two rows are sensitive to 150 GHz (bandwidth 31 GHz). Each detector is offset from its nearest neighbors by $\sim 16'$. ACBAR is mounted on the Viper telescope, a 2 m off-axis Gregorian telescope at the geographical South Pole. The telescope produces beams with FWHM of 4–5' in all frequency bands. Through the use of a chopping flat mirror, the

telescope sweeps the beams across the sky at frequencies up to several Hz, with peak-to-peak amplitude of $\sim 3^\circ$ in the azimuthal direction. The results presented in this paper are derived from the data taken with a chopping frequency of 0.3 Hz. ACBAR has high resolution in spherical harmonic multipole l -space ($\Delta l \sim 100$) over a wide range of angular scales ($150 < l < 3000$), allowing precise measurements of the CMB power spectrum (K2004).

The observations used in this work began in late March of 2002 and continued through the end of July when the supply of liquid helium at the South Pole station was exhausted. There are about 200 data files spanning that period, each of which constitutes up to six hours of continuous observation. One six hour observation consists of approximately 300 “stares” each lasting about one minute. During a stare, the telescope tracks a fixed position on the sky while the chopper sweeps out a triangle wave in azimuth. Each of these stares falls into one of three categories: lead, main, or trail (LMT). Lead and trail stares are offset $\pm 3^\circ$ in RA from the main stares and have half the integration time that main stares do. Each LMT group of stares is offset in declination, so that the final dataset represents a rastered map of the sky. Kuo et al. (2004) produced a CMB angular power spectrum from the M-(L+T)/2 differenced map. However, for the purpose of this atmospheric study, LMT stares are not differenced and are treated identically.

4. DATA PROCESSING

The beams of the ACBAR array are swept in azimuth with a 0.3 Hz triangular oscillation. The amplitude of the waveform is 3° in azimuth when the telescope is pointed at the horizon. The timestream from the ACBAR detectors is binned into vectors, or data strips, s_i^p , $i = 1, 2, \dots, n$, each of which consists of $n = 128$ temperature measurements for array element p covering 3° on the sky. The data corresponding to sweeps in the right (positive AZ) or left (negative AZ) directions are binned separately, resulting in two data vectors from every complete chopper cycle. The data vectors are calibrated in RJ temperature units by referencing them to observations of the brightness temperature of Mars and Venus (Runyan et al. 2003).

Correlation matrices are calculated from the outer products of data vectors corresponding to different elements in the detector array and compared with the model for the atmosphere-induced correlations. By correlating data vectors from distinct array elements, we obtain cross-correlation matrices that have a significantly lower bias from noise power than the autocorrelation. To maximize the signal-to-noise ratio (SNR), we correlate all pairs of array elements within a particular frequency passband. The angular offsets between these pairs of array elements are listed in Table 1, and a schematic diagram of the pairs is presented in Fig. 3. Because there are twice as many array elements operating in the 150 GHz band, there are many more correlation matrices for that frequency passband.

The statistical correlation depends only on the relative displacement of the pairs of array elements. Therefore, we average the correlation matrices of all pairs with the same frequency band and displacement vector together in a single correlation matrix. In order to reduce the volume of data, we assume that the correlation is sta-

TABLE 1

Pair	$\Delta\phi$	$\Delta\epsilon$	n_{150}	$n_{219,274}$
A	$-16'$	$0'$	6	3
B	$-32'$	$0'$	4	2
C	$-48'$	$0'$	2	1
D	$0'$	$-16'$	4	0
E	$-16'$	$-16'$	3	0
F	$-32'$	$-16'$	2	0
G	$-48'$	$-16'$	1	0
H	$+16'$	$-16'$	3	0
I	$+32'$	$-16'$	2	0
J	$+48'$	$-16'$	1	0

NOTE. — Angular offset in azimuth ($\Delta\phi$) and elevation ($\Delta\epsilon$) between array elements used for the correlation analysis. The total number of correlation maps associated with each array displacement and chopper direction is listed for the 150 GHz (two rows of detectors) and 219, 274 GHz (one row of detectors each) data. The 219 and 274 GHz data contain only displacements in azimuth and have the same number of correlations maps; $n_{219,274}$ corresponds to either of the two detector rows.

tionary and average the matrices over a period of many sweeps. The rotation of the telescope with respect to the ground based wind vector places constraints on the acceptable period of time averaging. The fundamental length of time over which the correlations are averaged is one quarter of a data file or about 1.5 hours (see Section 5.2 for details). This procedure is repeated with the data from the opposite direction of chopper motion to yield two correlation matrices for each band, detector displacement vector, and time period. After removing modes that are susceptible to airmass gradient and chopper synchronous offsets (zeroeth, first, and second order polynomial) and subtracting the average of all the stares in the file from each stare, we compare the measured correlation matrices with those calculated from eq. [3].

The chopping mirror on the Viper telescope sweeps the optical beams at a constant angular speed $\pm\gamma$ (rad s^{-1}). At time zero ($t = 0$), a detector element measures sky

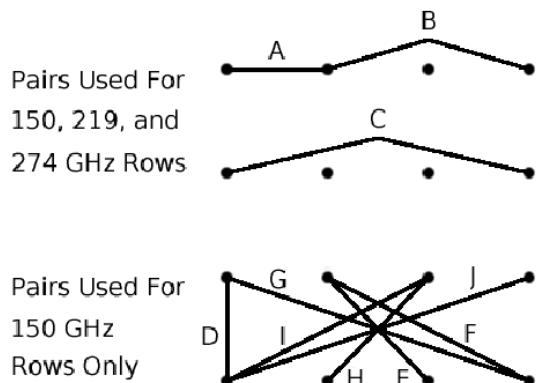


FIG. 3.— Schematic of ACBAR focal plane demonstrating an example of each array element pair correlation that has been used in the analysis. See Table 1 for a tabular representation of all possible pairs. Correlations are computed for all possible pairs of distinct array elements within a frequency passband. The letters A, B, C ... correspond to the array displacements in Table 1.

temperature T_1 in the direction (AZ, EL) = (ϕ, ϵ) . τ seconds later, another detector element (with position offset $\Delta\phi, \Delta\epsilon$) measures sky temperature T_2 in the direction of (ϕ', ϵ') . The correlation of T_1 and T_2 is $C(\theta)$ given by eq. [3], where the angular separation θ is

$$\begin{aligned} \theta &= \sqrt{(\phi' - \phi)^2 + (\epsilon' - \epsilon)^2} \\ &= \sqrt{(w_\phi \tau \mp \gamma \tau - \Delta\phi)^2 + (w_\epsilon \tau - \Delta\epsilon)^2}, \end{aligned} \quad (4)$$

and (w_ϕ, w_ϵ) are the components of the wind angular velocity in the direction of (ϕ, ϵ) . The wind linear velocity is related to the angular velocity by:

$$\begin{aligned} \frac{v_x}{h} &= -\frac{\sin \phi}{\sin \epsilon} w_\phi + \frac{\cos \phi}{\sin^2 \epsilon} w_\epsilon, \\ \frac{v_y}{h} &= \frac{\cos \phi}{\sin \epsilon} w_\phi + \frac{\sin \phi}{\sin^2 \epsilon} w_\epsilon. \end{aligned} \quad (5)$$

Note that the angular separation θ is measured on the ‘‘frozen’’ screen of atmospheric fluctuations. When $\Delta\phi = \Delta\epsilon = 0$, $C(\theta)$ becomes the autocorrelation function. One interesting implication of this scan strategy is that the observed atmospheric fluctuation signal depends on the direction of the chopper motion (a plus or minus sign in eq. [4]) with respect to the wind direction. Compared to a drift scan experiment ($\gamma = 0$), the fluctuation signal is suppressed when the beams and the wind move in the same direction, and enhanced when they move in the opposite directions. This effect is easily understood in the limit where $\gamma = w_\phi$, $w_\epsilon = 0$. The optical beams follow the frozen turbulence as it is blown across the sky and the AC-coupled bolometers will not detect any atmospheric signal. On the other hand, when the chopper goes in the opposite direction to the wind, the instrument will record an enhancement in atmospheric signal.

5. MODEL FITTING

The KT model given by eq. [2] is used to characterize the atmospheric fluctuation angular power spectrum. For each observation, we determine a set of parameters that minimizes the difference between the theoretical correlation function and the observed data. These parameters are defined in eqs. [2 – 5] and include the amplitude for each observing frequency, B_ν^2 ; a power law exponent, b ; and angular wind velocity in the x and y directions, v_x/h and v_y/h , respectively. As a result of the Earth’s rotation, the telescope tracks across the sky in azimuth, changing by 90° during the course of a six hour observation. Using eq. [5], we find the components of the prevailing wind angular velocity, v_x/h and v_y/h as functions of the wind velocity components in the telescope frame and the time during the observation (which sets ϕ , the azimuth).

To compare the parameterized model to the data, we first need to generate a theoretical correlation matrix, \mathcal{C} , from eq. [3]. We do this by discretizing the temporal lag τ in eq. [4] into n bins, where n is the length of each data vector being correlated—in our case, 128. If we denote τ_i as the discretized temporal lag associated with the sky temperature measurement in the direction of (ϕ, ϵ) and τ_j as the same quantity for a distinct detector in the direction of (ϕ', ϵ') , then the temporal lag between these two temperature measurements is $\tau = \tau_i - \tau_j$ and we can

generate the discrete, $n \times n$ correlation matrix \mathcal{C} from the correlation function as follows:

$$\mathcal{C}^{ij} = C(\theta(\tau, \Delta\phi, \Delta\epsilon)). \quad (6)$$

where $\Delta\phi = \phi' - \phi$ and $\Delta\epsilon = \epsilon' - \epsilon$. We perform an equivalent mode removal on \mathcal{C}^{ij} as was performed on the observed data, so that the theoretical and observed correlations can be directly compared. We calculate a χ^2 for the fit of the theoretical correlation matrix to the observed data for each frequency passband and unique correlation matrix:

$$\chi_{k,\nu}^2 = \frac{\sum_{i,j} (\mathcal{C}_{k,\nu,model} - \mathcal{C}_{k,\nu,data})^2}{\sigma_{k,\nu}^2}, \quad (7)$$

where $\sigma_{k,\nu}$ represents the intrinsic detector noise associated with the k^{th} correlation map for observation frequency ν . We compute the correlation matrices corresponding to the noise in a given 6 hour observation (denoted by $\mathcal{C}_{k,\nu,noise}$) as described in Section 4 with the difference that the data vectors for the detector pairs are drawn from the three possible pairs of 1.5 hour subfiles separated by at least 1.5 hours in time. We expect the atmosphere to be uncorrelated between these two measurements and the correlation should provide an accurate estimate of the noise. Finally, $\sigma_{k,\nu}$ is obtained from the variance of the k^{th} correlation matrix of frequency ν :

$$\sigma_{k,\nu}^2 = \sum_{i,j} (\mathcal{C}_{k,\nu,noise})^2 \quad (8)$$

The overall χ^2 used to determine the model parameters is given by

$$\chi^2 = \frac{\sum_{k,\nu} \chi_{k,\nu}^2 w_{k,\nu}}{\sum_{k,\nu} w_{k,\nu}}, \quad (9)$$

where $w_{k,\nu}$ represents the weight of the k^{th} correlation matrix found in column 4 ($\nu = 150$ GHz) or 5 ($\nu = 219$ or 274 GHz) of Table 1. For example, $k = 0$, $\nu = 274$ GHz corresponds to left- or right-going correlation matrices with angular offsets of $\Delta\phi = -16'$ and $\Delta\epsilon = 0'$. From Table 1, we see there are three pairs with this angular offset, meaning $w_{0,274} = 3$. $k = 1$, $\nu = 150$ GHz corresponds to left- or right-going correlation matrices with angular offsets of $\Delta\phi = -32'$ and $\Delta\epsilon = 0'$, so $w_{1,150} = 4$.

The lack of detector differences in the ϵ direction for the 219 and 274 GHz data results in a poor determination of this component of the wind velocity from this data alone. However, the 150 GHz data feature correlation matrices with angular offsets in both ϕ and ϵ directions, and can be used to obtain reliable wind velocity parameters. We simultaneously fit the data for all frequencies with the wind velocity to be constrained to be the same for all detector pairs. The 150 GHz data provides constraints on the ϵ component of the wind velocity. We use the IDL AMOEBA routine to perform the minimization and determine the best fit parameters for the KT model.

5.1. Correlation Matrix Fits

We begin by fitting the model parameters to the data divided in 1.5 hour segments. We find that the atmospheric fluctuations observed by ACBAR are well described by eqs. [3, 4] for about 93% of the data. A

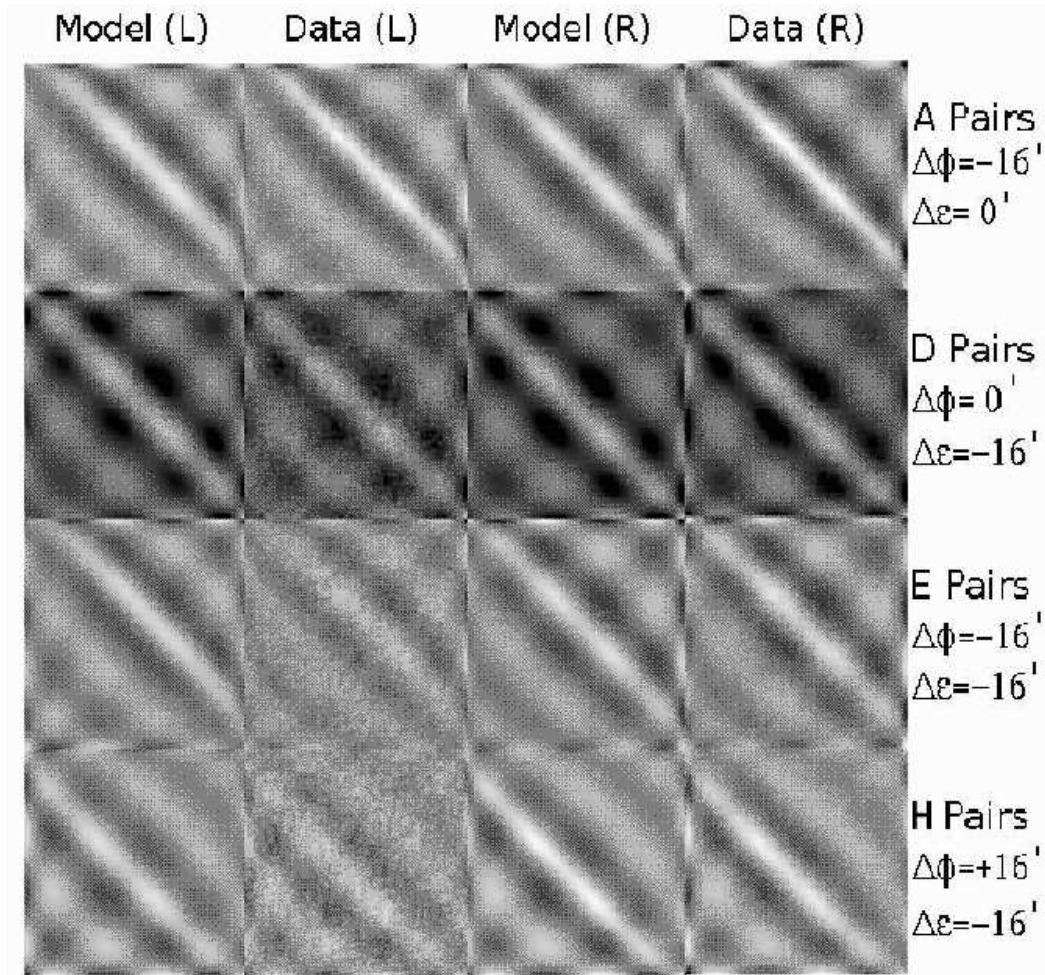


FIG. 4.— Correlation matrices produced by the model (1st and 3rd columns) as compared to the observed correlation matrices (2nd and 4th columns) for a 1.5 hour file of 150 GHz data from May 30, 2002. The two columns on the left correspond to a left-going motion of the chopper while the two columns on the right correspond to a right going sweep. The rows are a representative sampling of available angular displacements between 150 GHz array elements.

typical example of a good fit by the model is shown in Figs. 4 and 5. These figures show the theoretical and observed correlation matrices for a 1.5 hour data file obtained on 2002 May 30. The two columns on the left correspond to left-going sweeps of the telescope, while the two columns on the right represent the opposite direction. Fig. 5 shows a cross-section through the center of the correlation matrices presented in Fig. 4. This file has a particularly high azimuthal component of wind velocity and the cross-section plots demonstrate the difference in amplitude between the left-going and right-going sweeps. As described in Section 4, the sky noise is suppressed when the beam follows the wind (as seen in the left-going sweeps for this day), and enhanced when they move in the opposite directions.

One of the unique features of this work is that it appears possible—provided the KT model reasonably describes the data—to measure the atmospheric fluctuation power under nearly all atmospheric conditions, even during the best weather. As mentioned in Section 5, the intrinsic detector noise sets a fundamental limit to the smallest atmospheric fluctuation power that can be

measured. We characterize the noise in the fluctuation amplitude by fitting to the random correlations between detectors in time-separated sweeps. In Fig. 6, we plot the noise power amplitude vs. the power amplitudes found for the correlations within the sweeps. The line represents a SNR of approximately one. Nearly all of the data lie above this line, indicating that the amplitude of the fluctuations is not limited by an instrumental noise floor and that the amplitude of the fluctuation power is typically measured with high accuracy (median SNR is 140) under nearly all observing conditions.

We identify the observations that do not provide adequate fits to the KT model from the χ^2 defined by eq. [9]. We find that 7% of the total observations fail to measure the KT model amplitude with $\chi^2 < 20 * median(\chi^2)$. In general, the poor fits are not due to a lack of fluctuation power, but rather the presence of fluctuations that cannot be described by our assumed model. We have broken these files into smaller time periods and find no improvement in the fits, indicating that it is not a problem with the fit parameters changing in time. Two possible explanations are that either the observed spatial fluctuations

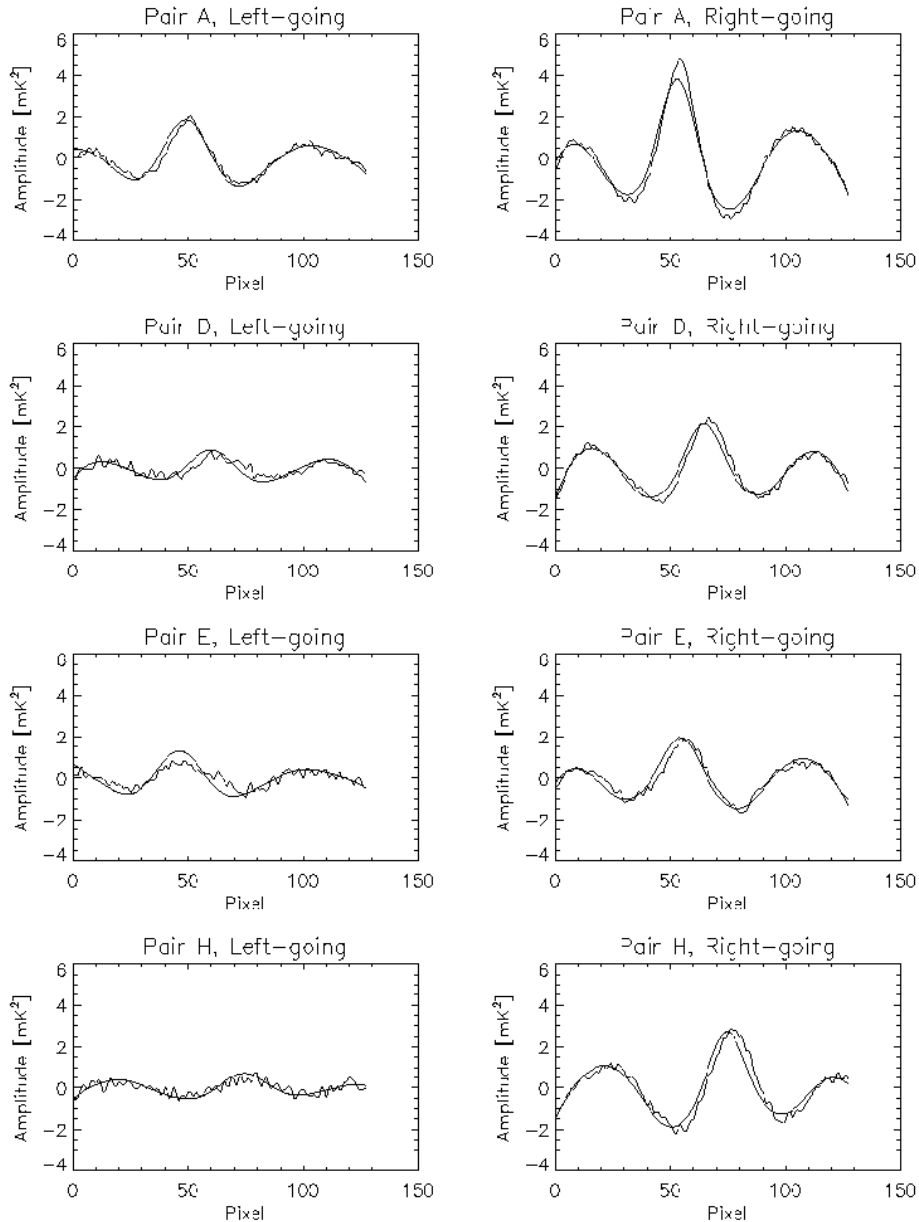


FIG. 5.— Cross-Sectional plots of the observed correlation matrices shown in Fig. 4 with the model fit overplotted. The cross-section is taken in the horizontal direction through the center of the correlation matrix, and serves as a demonstration of the quality of the fit. Due to the high wind velocity, the sky noise is suppressed for the chopper moving in the same direction as the wind (left column) or enhanced for motion in the opposite direction (right column).

do not obey a Kolmogorov power law at this time, or the atmospheric structure is not frozen on the timescale of a sweep. Another more likely explanation is that a significant fraction of the observed power is coming from a layer in the near field of the telescope, which we estimate to be approximately 500 m. In this case, the assumptions made in the derivation of the theoretical correlation function are not valid. The data with poor fits are typically associated with very large fluctuation amplitudes, and are therefore likely to be due to a severe storm.

5.2. Timescale of Disturbances

By averaging the correlation matrices over longer periods of time, it is possible to measure the model pa-

rameters (particularly the wind velocity) with higher accuracy. However, it is important that the atmospheric conditions remain constant over the period for which the correlations are averaged. The CMB observations we are using for this analysis cover 6 hours; this sets a practical upper limit to the averaging. In this section, we show that the atmospheric conditions are typically quite stable over the course of a six hour observation.

Each of the six hour data files is subdivided into four 1.5 hour subfiles. Model parameters are determined for each of the subfiles from fits to the 150 GHz data. To reduce computing time, we fit only to the 150 GHz data for the tests described here and in Section 5.3. In Fig. 7, we show the correlation between the power amplitudes

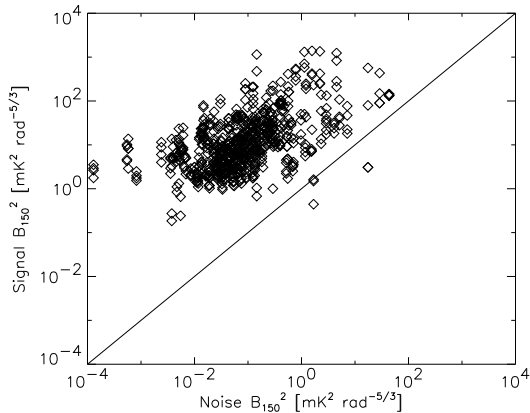


FIG. 6.— A graphical representation of the SNR in the determination of the fluctuation power amplitude. On the y-axis, we plot the mean fluctuation amplitude found from the individual 1.5-hour segments of a 6 hour data file. The x-axis is the amplitude computed from the correlation between detector timestreams separated by at least 1.5 hours within a given 6-hour observation. The diagonal line represents equal fluctuation power amplitude for the signal and noise correlations. The fluctuation amplitude is recovered with high SNR in nearly all files. In fact, the median SNR is 140.

determined for the 1st and 4th quarters of each file. The strong correlation indicates that the atmospheric fluctuation power is relatively consistent in time and we are justified in fitting a single fluctuation power to a six hour data set. Due to the rotation of the telescope with respect to the prevailing wind direction as it tracks a source, we cannot simply average the correlation matrices over the entire 6 hour observation. Instead, we project a constant ground-based wind velocity into the appropriate telescope frame for each of the quarters of the file. The minimization for the model parameters then proceeds as for a single file; however, we use the combined χ^2 for all four files as a metric of goodness of fit.

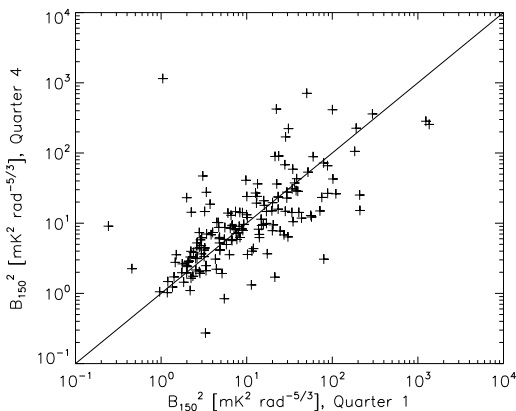


FIG. 7.— Correlation of brightness fluctuation power amplitude over the span of a six hour observation. We show correlation between B_{150}^2 measured from first and fourth quarters of a six hour data file. The strong correlation implies that that brightness fluctuation power typically remains constant over a time period of at least six hours.

5.3. Power Law Exponent

We can determine the exponent of the KT power law for those observations in which we measure the fluctuations with high SNR. In Fig. 8, we show the distribution of measured values of the power law exponent over the course of the winter where the mean exponent for that period of time is $b = 4.1 \pm 0.8$. If we restrict the observations to those with above-median SNR, we find that the distribution of exponents is described by $b = 3.9 \pm 0.6$. In both cases, our results are consistent with those expected for the KT model in the 3D regime. For the rest of our analysis, we have set the exponent of the KT power law equal to $11/3$. This assumption is physically motivated and increases the stability of the model-fitting by removing one of the free parameters.

6. RESULTS

In this Section, we describe the basic results of the fits of the KT model to the observed data. As described in Section 5.2, the stability of the atmospheric conditions allows us to determine the model parameters for an entire six hour observation. Although the fluctuation amplitude is determined with high SNR in each of the file quarters, fitting to all four simultaneously significantly improves the determination of the KT exponent and wind velocity components. Unless otherwise noted, the following results are found assuming that the model parameters are constant over a six hour data file. The amplitudes for the fluctuation power are free to vary in each of the bands, while the wind angular velocity is constrained to be constant across all bands. For the 219 and 274 GHz rows, this greatly improves the stability of the results.

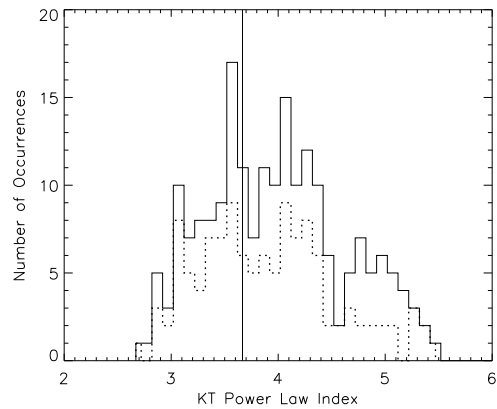


FIG. 8.— Distribution of the measured KT power law exponent values for the Austral winter of 2002. Observations that do not fit the KT power law (according to the χ^2 cut described in Section 5.1) are not included in this distribution. The solid line shows the distribution of exponents for all good fits to the KT model; the mean of this distribution is 4.1 ± 0.8 . The dotted lines shows the distribution of exponents for all observations with below-mean χ^2 for the fit to the KT model; the mean of this distribution is 3.9 ± 0.6 . In both cases, the results agree with the theoretical KT power law for small angular scales, which is shown as a vertical line. For the rest of the analysis, we fix the exponent at the expected value of $b = 11/3$ to remove the degeneracy between the amplitude and exponent of the power law.

6.1. Amplitude Measurements

We have used fits to the KT model to measure the brightness fluctuation power amplitude of the atmosphere over a four month period from late March through July 2002. Although the measurements were made at a range of elevations, the results have been normalized in terms of observations at the zenith. The results of this analysis for 150 GHz data are shown in Fig. 9. The atmospheric brightness fluctuation power is relatively stable, with roughly 60% of the data falling between $B_{150}^2 = 5 - 40 \text{ mK}^2 \text{ rad}^{-5/3}$. This is in contrast to the findings of LH2000, who reported a bimodal distribution of brightness fluctuation power for the Austral summer of 1996. Solar heating and associated weather during the summer is one possible cause of this difference.

We have performed a similar analysis for the 219 and 274 GHz data. The emissivity of water vapor increases as a function of frequency, resulting in higher amplitude fluctuations at higher frequencies. In Fig. 10, we compare the amplitudes found from the 219 GHz observations with those found at 150 GHz. The degree of correlation is a consequence of the high SNR of all the measurements and is similar to that found between the 150 and 274 GHz data. The brightness fluctuation power amplitude at 274 (219) GHz is approximately 7.4 (3.7) times greater than at 150 GHz. In Fig. 11, we show a Cumulative Distribution Function (CDF) of the brightness fluctuation power for each of the three frequency bands. From these distributions, we extract upper limits to the quartiles in brightness fluctuation power amplitude and list them in Table 2. We compensate for the 7% of the data that do not fit the KT model by assuming that all the poor KT fits have amplitudes larger than the largest good KT fit. The 27th, 54th, and 81st percentiles then serve as upper limits to the quartiles of the full distribution.

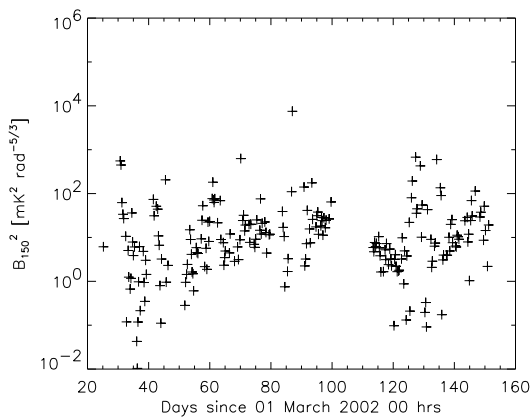


FIG. 9.— The brightness fluctuation power, in $\text{mK}^2 \text{ rad}^{-5/3}$, for 4 months of 150 GHz ACBAR observations at the South Pole. Each data point represents about six hours of continuous observations normalized to observations at the zenith angle. Approximately 7% of the data exhibit anomalous turbulence which are not well fit by a KT model, and are not shown here. We assume that these data always have amplitudes larger than data which can be modeled with a KT power law and adjust our amplitude distributions accordingly. Mechanical problems with the instrumentation limited the acquisition of data for days 100-112.

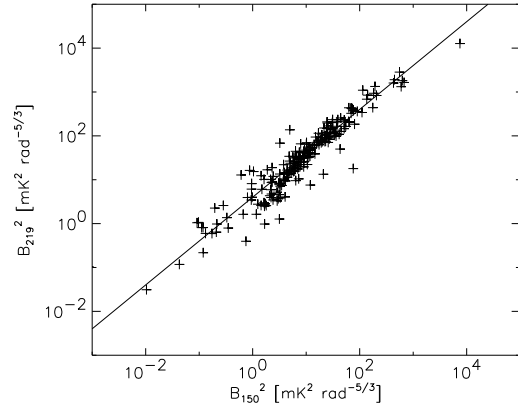


FIG. 10.— The fluctuation power amplitudes determined at 150 GHz vs. 219 GHz. The high degree of correlation is a result of the large SNR in the determination of the amplitudes and the robust fits to the model. A similar plot for the 150 GHz vs. 274 GHz results is qualitatively identical.

The median fluctuation power amplitudes for each of the bands are listed in Table 3. For comparison, we also list the median fluctuation power measured by the Python experiment from the paper of LH2000. Due to the increase in atmospheric brightness with frequency and the higher sensitivity of the instrument, the ACBAR measurements are significantly more sensitive to water vapor than those made with Python. This sensitivity is helpful in characterizing the much more quiet winter atmosphere.

We have used a model for the spectrum of atmospheric water vapor to compare the results from the four frequency bands covered by ACBAR and Python. The At-

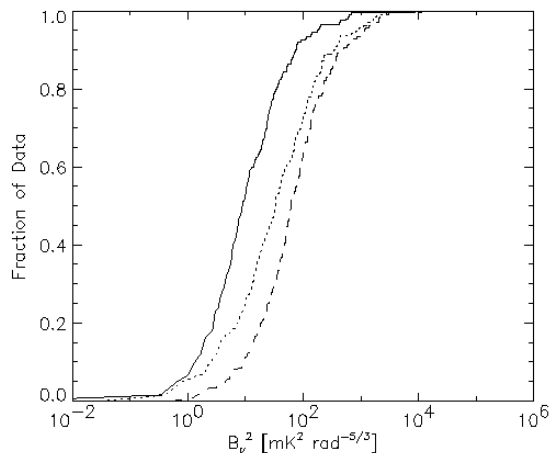


FIG. 11.— The cumulative distribution functions of brightness fluctuation power amplitude (in Rayleigh-Jeans temperature units) for the entire winter season of ACBAR observations. The solid, dotted, and dashed lines represent 150 GHz, 219 GHz, and 274 GHz data, respectively. The 7% of the data that is poorly fit by a KT model is not included in this plot. The upper limits to amplitude quartiles given in Table 2 have been calculated from these distributions.

mospheric Transmission (AT)⁶ code is used to produce spectra corresponding to winter conditions at the South Pole with 0.25 mm water vapor as well as 0.0 mm water vapor. The difference of these two spectra gives an estimate of the emission due to water vapor as a function of frequency. The emission spectrum of atmospheric water vapor is shown in Fig. 12, with the four passbands shown in gray. We integrate over the passbands to obtain the effective opacity τ'_{band} due to 0.25 mm water vapor for each of the observing frequencies; 40, 150, 219, and 274 GHz. We then scale the fluctuation power amplitude for each of the bands by the square of the ratio of the water vapor opacities to normalize the results to the equivalent power that would have been seen in simultaneous observations at 150 GHz.

$$\text{Equivalent } B_{150}^2 = B_{\nu}^2 \left(\frac{\tau'_{150}}{\tau'_{\nu}} \right)^2$$

Given a perfect understanding of the ACBAR bands, an accurate water vapor spectrum, and the validity of the assumption that the atmosphere is optically thin, we expect the scaled fluctuation amplitudes for the ACBAR measurements to be identical. The equivalent brightness fluctuation power amplitudes for the Python observations made during the Austral summer are more than 10 times higher than those for the ACBAR measurements made during the Austral winter. We attribute this difference largely to the lower water vapor content of the atmosphere during the winter, although the stability of the atmosphere may also be improved in the winter.

The measurements of the fluctuation amplitude made with the Python experiment and reported in LH2000 are given in terms of $Ah^{8/3}$, while the ACBAR results are given in terms of $B_{\nu}^2 = Ah^{5/3}$. In order to compare the results of the experiments, it is necessary to divide the numbers from LH2000 by the altitude of the layer containing the fluctuations. This additional factor of h was introduced by the authors of LH2000 so that the data would be easier to insert into a set of approximate analytic expressions predicting the level of residual atmospheric noise in different classes of observations. However, these expressions are only valid in the limit of long averaging times, which are not appropriate for many observing strategies. B_{ν}^2 is what is actually measured by the experiments, and is therefore more fundamental and useful than $Ah^{8/3}$. In Section 6.2 we show that the scale height of the fluctuations is consistent with the distribution of precipitable water vapor. Should one desire to compute $Ah^{8/3}$ from the ACBAR data, multiply B_{ν}^2 by the water vapor pressure weighted altitude, $h = 1300$ m.

Measurements of the sub-mm atmospheric opacity are an important monitor of observing conditions. We have investigated the correlation of the measured fluctuation amplitude with both the sub-mm opacity (τ) and the variance of the opacity (σ_{τ}). The sub-mm tipper (sky brightness monitor) on the AST/RO experiment (Radford 2002) at the South Pole measures the 350 μm zenith opacity and atmospheric temperature every 15 minutes. The 350 μm atmospheric opacity is much larger than 150 GHz opacity, but they are both dominated by water vapor and, therefore, scale nearly linearly. We bin

TABLE 2

Percentile	27th	54th	81th
150 GHz	3.7	10.	37.
219 GHz	11.	38.	160
274 GHz	28.	74.	230

NOTE. — Upper limits to quartiles of fluctuation amplitude (B_{ν}^2) for 150, 219, and 274 GHz data in Rayleigh-Jeans temperature units of $\text{mK}^2 \text{ rad}^{-5/3}$. These values are calculated from the cumulative distribution functions shown in Fig. 11. We report the 27th, 54th, and 81st percentiles, because the distribution from which they are calculated does not include the 7% of non-KT observations. We assume that each of the non-KT observations has an amplitude larger than the largest KT observation, the values in this table represent upper limits to the 25th, 50th, and 75th percentiles of the full distribution.

the opacity values from the tipper to match the length of the observation (typically about six hours); the fractional variance in opacity over that time-span (σ_{τ}/τ) is usually less than 10%. Fig. 13 shows the fluctuation power amplitude versus the square of the opacity, τ^2 . The correlation between the fluctuation power amplitude and the variance of the opacity is similarly weak. These results imply that τ and σ_{τ} are not, by themselves, an adequate judge of the stability of the atmosphere on timescales relevant to the ACBAR measurements.

6.2. Wind Velocity and Scale Height

In general, the angular speed of the chopper is higher than the effective angular speed of the fluctuations produced by wind. Therefore, the effect of the wind velocity on the observed correlations is typically sub-dominant to the effect of the chopper motion. In practice, the amplitude of the fluctuations can usually be recovered with high SNR even when very poor constraints can be placed on the wind velocity. However, in cases where the fluctuations are measured with high SNR, the wind angular velocity can be accurately recovered. This wind angular

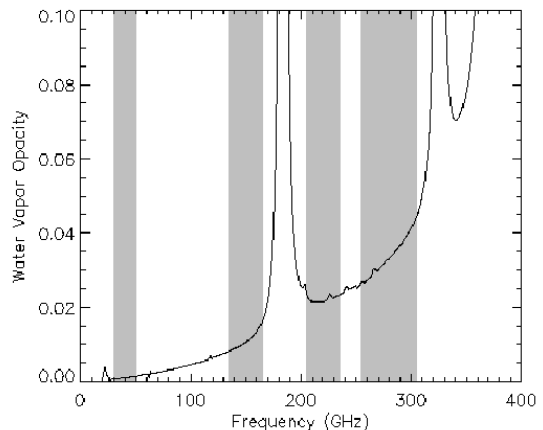


FIG. 12.— Water vapor emission spectrum obtained from the difference between a “wet” spectrum with 0.25 mm input water vapor and a “dry” spectrum with 0.0 mm water vapor. Approximate frequency passbands of the Python (40 GHz) and ACBAR (150, 219, 274 GHz) experiments are shown with grey rectangular bars.

⁶ Airhead Software, Boulder CO

TABLE 3

Frequency	40 GHz	150 GHz	219 GHz	274 GHz
Median B_ν^2 [$\text{mK}^2 \text{ rad}^{-5/3}$] (CMB units)	0.90	31.	350	2.0×10^3
Median B_ν^2 [$\text{mK}^2 \text{ rad}^{-5/3}$] (RJ units)	0.84	10.	38.	74.
Equivalent B_ν^2 for 150 GHz	11.	1.0	0.92	0.86

NOTE. — Comparison of median brightness fluctuation power for measurements with the ACBAR and Python (see LH2000) experiments. The results are listed in both Rayleigh-Jeans and CMB temperature units. Clearly, RJ units are more natural for comparing between different bands, however, we include the CMB normalization in order to facilitate the prediction of noise in future experiments. We use a water vapor spectrum to normalize the atmospheric fluctuation power for the Python 40 GHz and ACBAR 219, 274 GHz observations to the equivalent power for the 150 GHz ACBAR band. The data for the three ACBAR bands were taken simultaneously and, therefore, the equivalent 150 GHz amplitudes should be roughly identical. The Python numbers are computed from Table 1 in LH2000 assuming the average altitude of the fluctuations, $h_{av} = 1000\text{m}$. The order of magnitude higher equivalent fluctuation power for the extrapolated 40 GHz Python results is a result of the lower precipitable water vapor and increased stability of the atmosphere during the winter at the South Pole.

velocity can be combined with radiosonde measurements of wind linear velocity to estimate the scale height from which the atmospheric fluctuation power originates.

Data files with a χ^2 (as described by eq. [9]) below the median are selected as being likely to result in reliable wind velocities. The wind angular velocities for each 1.5-hour file are found in a coordinate system that is fixed with respect to the direction the telescope is pointing. However, over the course of a long data file, the telescope tracks a source through a considerable range of angle and this motion must be taken into account. The transformation described by eq. [5] ties the local wind velocities for each 1.5-hour data set into a single wind velocity with respect to the ground constant over the entire data file. We are justified in doing this because both the measurements of the wind angular velocities with ACBAR and the wind linear velocities with radiosondes show that the wind is typically quite constant over a 6-hour data file.

The ACBAR measurements of wind angular velocity can be combined with radiosonde linear velocity and water vapor pressure as a function of elevation to determine the mean elevation (h) from which the fluctuations orig-

inate:

$$h = \frac{v_{rs}}{\omega_{Acbar}} \quad (10)$$

where v_{rs} is defined as

$$v_{rs} = \frac{\int_0^\infty v(z)P_{wv}(z)dz}{\int_0^\infty P_{wv}(z)dz}, \quad (11)$$

$v(z)$ is the wind linear speed from the radiosonde data, $P_{wv}(z)$ the water vapor pressure (calculated in Section 2.1), and z the altitude above ice level. Fig. 14 is a histogram of the altitude of the inferred layer giving rise to the measured fluctuations. The results are in reasonable qualitative agreement with the average water vapor pressure weighted altitude calculated from radiosonde data shown in Fig. 1. This provides further confidence that we understand the source of the fluctuations and have accurately characterized them.

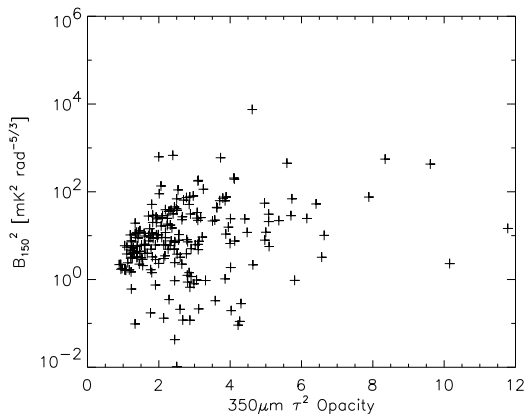


FIG. 13.— Fluctuation power amplitude versus $350 \mu\text{m}$ opacity-squared. The weak correlation between B_{150}^2 and τ^2 implies that τ alone is not a reliable indicator of atmospheric fluctuations.

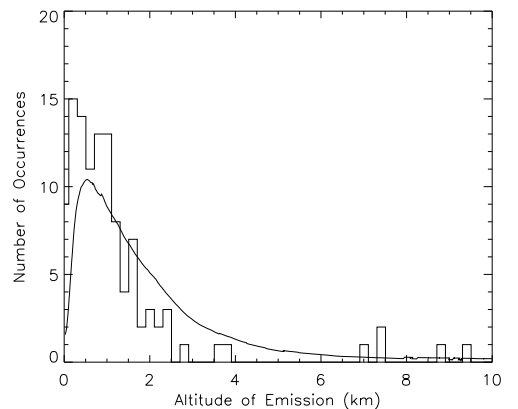


FIG. 14.— Distribution of the inferred altitudes for the atmospheric fluctuations. These results are computed from the ratio of the ACBAR (below-median χ^2 150 GHz data) wind angular velocities to the radiosonde derived water vapor pressure weighted wind linear velocities. The results are consistent with the average water vapor pressure profile calculated from the data shown in Fig. 1 and reproduced here as a smooth line. The mean inferred scale height of the emission is $\sim 1.3\text{km}$.

7. CONCLUSIONS

We have produced a detailed characterization of the millimeter wavelength atmospheric fluctuations at the South Pole during the Austral winter of 2002. By correlating the signals between pairs of elements in the ACBAR bolometer array it is possible to reduce the effect of uncorrelated detector noise such that the atmospheric fluctuations can be measured with high SNR even for the lowest fluctuation amplitudes. We found that a KT model is an accurate description of the atmospheric fluctuation power $\sim 93\%$ of the time. The median exponent of the power law is found to be consistent with the theoretically expected value $b = 11/3$. For the bulk of the analysis, we fix the exponent to $11/3$ in order to improve the SNR in the determination of the other model parameters. We found upper limits to the quartiles of the 150 GHz atmospheric fluctuation power for the four winter months of observation to be [3.7, 10., 37] $\text{mK}^2 \text{rad}^{-5/3}$. The scaling between the measured fluctuation power amplitudes for each of the three ACBAR frequencies is consistent with that expected for emission from water vapor. We used this fact to compare our results with those of LH2000 made at 40 GHz with the Python experiment in the Austral summer of 1996. Assuming that the scale heights of the fluctuations in the summer and winter are equivalent, the median fluctuation power found with ACBAR observations in the Austral winter corresponds to a fluctuation power amplitude ~ 10 times smaller than that found with Python during the Austral summer. From the analysis in LH2000, this implies that the atmospheric fluctuation power at the South Pole in the Austral winter is at least ~ 30 times

smaller than that at the ALMA site in the Chilean Andes. In addition, we found that the fluctuation power amplitude is only weakly correlated with atmospheric opacity or its variance on 15 minute timescales. Therefore, for experiments sensitive to atmospheric fluctuations, periodic measurements of optical depth do not appear to be an adequate characterization of an astronomical site. Finally, we determined the wind angular velocity for each of the observations with below median χ^2 and compared our value to the wind linear velocities obtained by radiosonde measurements to determine the scale height of the observed atmospheric fluctuations. We find that the inferred scale heights for each of the data files roughly fall within the 300 m–2000 m range suggested by the radiosonde water vapor pressure profiles.

We believe this work provides a fairly complete picture of the fluctuation power in the atmosphere above the South Pole. Already these results are being used to compare potential observation strategies for the 10-meter South Pole Telescope, which will be deployed in 2007. We anticipate that similar studies to that presented here, will be performed with data from other array receivers in order to compare quantitatively the atmospheric stability of observing sites.

The authors gratefully acknowledge the contributions of the entire ACBAR/Viper team in the construction, maintenance, operation, and calibration of the experiment. We would also like to thank Nils Halverson and Tom Crawford for their careful reading of an early draft of this work and their helpful suggestions for its improvement. This work has been supported by the NSF office of polar programs grant OPP-0091840.

APPENDIX

PROJECTED POWER SPECTRUM

Here we derive the instantaneous angular power spectrum, given the three dimensional temperature-density fluctuation spectrum. The thermodynamic temperature of the atmosphere is on the order of 200 K, hence the Rayleigh-Jeans law is a good approximation at mm wavelengths. In the optically thin limit and under the condition of local thermodynamic equilibrium, the specific radiation is proportional to the line of sight integration of the light emitting elements. Therefore, we can define the effective temperature $T_E(\mathbf{r})$, such that the brightness temperature T_B along $\hat{\mathbf{r}} \equiv \mathbf{r}/r$ is given by

$$T_B = \int T_E \kappa dr ,$$

where κ is the opacity/thickness of the turbulent layer for millimeter wave photons. We assume that T_E includes both the physical temperature variations and density variations. The angular correlation function for T_B can then be written as

$$\begin{aligned} C(\theta) &\equiv \langle T_B(\theta) \cdot T_B(0) \rangle = \int_{h/\sin \epsilon}^{(h+\Delta h)/\sin \epsilon} dz \int_{h/\sin \epsilon}^{(h+\Delta h)/\sin \epsilon} dz' \kappa^2 \langle T_E(x, y, z') T_E(0, 0, z) \rangle \\ &= \int_{h/\sin \epsilon}^{(h+\Delta h)/\sin \epsilon} dz \int_{h/\sin \epsilon}^{(h+\Delta h)/\sin \epsilon} dz' \kappa^2 C_{3D}(x, y, z' - z) . \end{aligned}$$

Fig. A15 shows the coordinate system used in this calculation. In the small angle regime, the angular power spectrum is the Fourier transform of the angular correlation function, which can be derived from the 3-D correlation function, which in turn is the 3-D Fourier transform of the 3-D PSD:

$$\begin{aligned} P(\alpha_x, \alpha_y) &= \iint d\theta_x d\theta_y e^{-2\pi i(\alpha_x \theta_x + \alpha_y \theta_y)} C(\theta) \\ &= \iint d\theta_x d\theta_y \int_{h/\sin \epsilon}^{(h+\Delta h)/\sin \epsilon} dz \int_{h/\sin \epsilon}^{(h+\Delta h)/\sin \epsilon} dz' \kappa^2 e^{-2\pi i(\alpha_x \theta_x + \alpha_y \theta_y)} C_{3D}(x, y, z' - z) \end{aligned}$$

$$= \iint d\theta_x d\theta_y \int_{h/\sin \epsilon}^{(h+\Delta h)/\sin \epsilon} dz \int_{h/\sin \epsilon}^{(h+\Delta h)/\sin \epsilon} dz' \int d^3 k' \kappa'^2 \cdot e^{-2\pi i(\alpha_x \theta_x + \alpha_y \theta_y)} \cdot e^{2\pi i \mathbf{k}' \cdot \Delta \mathbf{x}} P_{3D}(k'),$$

with $\alpha_i \theta_i = k_i x_i$. Carrying out the all the integrals except for dk'_z , we have

$$P(\alpha_x, \alpha_y) = \left(\frac{h}{\kappa \sin \epsilon} \right)^{-2} \int_{-\infty}^{\infty} dk'_z P_{3D}(k_x, k_y, k'_z) \frac{\Delta h^2}{\sin^2 \epsilon} \left[\frac{\sin^2(\pi k'_z \Delta h / \sin \epsilon)}{\pi^2 k'^2_z \Delta h^2 / \sin^2 \epsilon} \right] \\ \approx \left(\frac{h}{\kappa \sin \epsilon} \right)^{-2} \int_{-\sin \epsilon / 2 \Delta h}^{\sin \epsilon / 2 \Delta h} dk'_z P_{3D}(k_x, k_y, k'_z) \frac{\Delta h^2}{\sin^2 \epsilon} \approx P_{3D} \left(\frac{\alpha_x}{h / \sin \epsilon}, \frac{\alpha_y}{h / \sin \epsilon}, 0 \right) \frac{\Delta h}{\sin \epsilon} \left(\frac{h}{\kappa \sin \epsilon} \right)^{-2}. \quad (\text{A1})$$

In the last two steps, the stationary phase approximation is used. Eq. [A1] states that the projected power spectrum obeys the same 3-D KT power law, $k^{-11/3}$, and its RMS is proportional to the square root of the path length through the turbulent layer, as would be expected.

With $P_{3D} \propto k^{-11/3}$, eq. [A1] implies that

$$P(\alpha) = B_\nu^2 \sin(\epsilon)^{-8/3} (\alpha_x^2 + \alpha_y^2)^{-11/6}. \quad (\text{A2})$$

Comparing this expression with eq.[13] in LH2000, we can see that;

$$B_\nu^2 = A h_{av}^{5/3},$$

and has units of $\text{mK}^2 \text{ rad}^{-5/3}$.

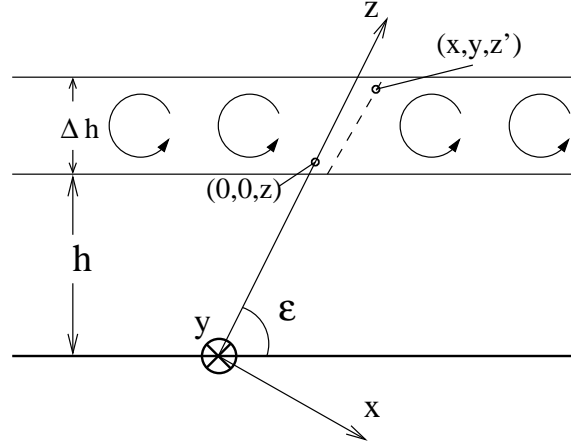


FIG. A15.— The coordinate system for the angular power spectrum derivation given in the appendix.

REFERENCES

- Chamberlin, R. A. & Bally, J. 1994, *Appl. Opt.*, 33, 1095
 Crill, B. P., Ade, P. A. R., Artusa, D. R., Bhatia, R. S., Bock, J. J., Boscaleri, A., Cardoni, P., Church, S. E., Coble, K., de Bernardis, P., de Troia, G., Farese, P., Ganga, K. M., Giacometti, M., Haynes, C. V., Hivon, E., Hristov, V. V., Iacoangeli, A., Jones, W. C., Lange, A. E., Martinis, L., Masi, S., Mason, P. V., Mauskopf, P. D., Miglio, L., Montroy, T., Netterfield, C. B., Paine, C. G., Pascale, E., Piacentini, F., Polenta, G., Pongetti, F., Romeo, G., Ruhl, J. E., Scaramuzzi, F., Sforza, D., & Turner, A. D. 2003, *ApJS*, 148, 527
 Kovac, J. M., Leitch, E. M., Pryke, C., Carlstrom, J. E., Halverson, N. W., & Holzzapfel, W. L. 2002, *Nature*, 420, 772
 Kuo, C. L., Ade, P. A. R., Bock, J. J., Cantalupo, C., Daub, M. D., Goldstein, J. H., Holzzapfel, W. L., Lange, A. E., Lueker, M., Newcomb, M., Peterson, J. B., Ruhl, J., Runyan, M. C., & Torbet, E. 2004, *ApJ*, 600, 32
 Lane, A. P. 1998, in *ASP Conf. Ser. 141: Astrophysics From Antarctica*, 289+
 Lay, O. P. 1997, *A&AS*, 122, 535
 Lay, O. P. & Halverson, N. W. 2000, *ApJ*, 543, 787
 Marks, R. D. 2002, *A&A*, 385, 328
 Marks, R. D., Vernin, J., Azouit, M., Manigault, J. F., & Clevelin, C. 1999, *A&AS*, 134, 161
 Radford, S. 2002, in *ASP Conf. Ser. 266: Astronomical Site Evaluation in the Visible and Radio Range*, 148+
 Runyan, M. C., Ade, P. A. R., Bhatia, R. S., Bock, J. J., Daub, M. D., Goldstein, J. H., Haynes, C. V., Holzzapfel, W. L., Kuo, C. L., Lange, A. E., Leong, J., Lueker, M., Newcomb, M., Peterson, J. B., Reichardt, C., Ruhl, J., Sirbi, G., Torbet, E., Tucker, C., Turner, A. D., & Woolsey, D. 2003, *ApJS*, 149, 265
 Taylor, G. I. 1938, *Proc. R. Soc. Lond. A*, 164, 476
 Travouillon, T., Ashley, M. C. B., Burton, M. G., Storey, J. W. V., & Loewenstein, R. F. 2003, *A&A*, 400, 1163
 Wollack, E. J., Devlin, M. J., Jarosik, N., Netterfield, C. B., Page, L., & Wilkinson, D. 1997, *ApJ*, 476, 440